High Frame-Rate, High Resolution Ultrasound Imaging with Multi-Line Transmission and Filtered-Delay Multiply And Sum Beamforming

Giulia Matrone, *Member, IEEE*, Alessandro Ramalli, Alessandro Stuart Savoia, *Member, IEEE*, Piero Tortoli, *Senior Member, IEEE*, and Giovanni Magenes, *Member, IEEE*

Multi-Line Transmission (MLT) was recently demonstrated as a valuable tool to increase the frame rate of ultrasound images. In this approach, the multiple beams that are simultaneously transmitted may determine cross-talk artifacts that are typically reduced, although not eliminated, by the use of Tukey apodization on both transmission and reception apertures, which unfortunately worsens the image lateral resolution.

In this paper we investigate the combination, and related performance, of Filtered-Delay Multiply And Sum (F-DMAS) beamforming with MLT for high frame-rate ultrasound imaging. F-DMAS is a non-linear beamformer based on the computation of the receive aperture spatial autocorrelation, which was recently proposed for use in ultrasound B-mode imaging by some of the authors. The main advantages of such beamformer are the improved contrast resolution, obtained by lowering the beam side lobes and narrowing the main lobe, and the increased noise rejection. This study shows that in MLT images, compared to standard Delay And Sum (DAS) beamforming including Tukey apodization, F-DMAS beamforming yields better suppression of cross-talk and improved lateral resolution. The method's effectiveness is demonstrated by simulations and phantom experiments. Preliminary *in vivo* cardiac images also show that the frame rate can be improved up to 8-fold by combining F-DMAS and MLT without affecting the image quality.

***Index Terms*—Filtered-delay multiply and sum beamforming, high frame-rate ultrasound imaging, multi-line transmission**

Manuscript received August 29, 2016.

This work has been partially supported by the National governments and the European Union through the ENIAC JU under grant agreement number 324257 (DeNeCoR Project).

This paper has supplementary downloadable material available at http://ieeexplore.ieee.org, provided by the authors. This includes two multimedia AVI format movie clips, which show an animated version of the 4-MLT and 8-MLT *in vivo* heart images in Fig. 5, together with the recorded ECG signal. This material is 35.2 MB in size.

G. Matrone and G. Magenes are with the Dipartimento di Ingegneria Industriale e dell'Informazione, Università degli Studi di Pavia, 27100 Pavia, Italy (corresponding author e-mail: giulia.matrone@unipv.it).

A. Ramalli and P. Tortoli are with the Dipartimento di Ingegneria dell'Informazione, Università degli Studi di Firenze, 50121 Florence, Italy.

A. S. Savoia is with the Dipartimento di Ingegneria, Università degli Studi Roma Tre, 00146 Rome, Italy.

I. INTRODUCTION

ULTRASOUND B-mode imaging is typically based on a line-by-line scan of the region of interest. Unfortunately, this principle of operation, combined with the limited speed of sound in tissues ($c \approx 1540$ m/s), sets an upper bound to the frame rate, which is inversely proportional to the number of scan lines and to the maximum depth investigated.

Achieving a high frame rate is crucial in many applications. For example, a system able to capture the heart motion and related rapid events could be important for a more accurate diagnosis [1] [2]. The frame rate is even more critical in 3D/4D imaging, where the number of scan lines included into a volume, is in the order of thousands [3].

Recently, the transmission of a single plane wave or, more in general, of an unfocused wave, has been proposed to achieve up to 10000 frames per second (fps) [4] [5]. Such transmission must be coupled, on the receiver side, to parallel beamforming [6] [7], also called Multi-Line Acquisition (MLA), which consists in the simultaneous formation of multiple adjacent scan lines. However, the transmission of unfocused waves leads to poor signal-to-noise ratio (SNR) and image resolution, which can be compensated for by coherently compounding the images acquired using differently steered waves [8] [9].

Another approach, which can be possibly combined with MLA [10], is called Multi-Line Transmission (MLT) [11] and consists in simultaneously transmitting multiple focused beams into different directions. In order to do so, the transducer excitation signals, that would be required to generate each of the concurrent steered beams, are properly delayed and then superimposed. The problem with this technique is that cross-talk artifacts are likely to arise due to the interactions among the beams, both in transmission (TX) and reception (RX). This issue has been addressed by several works in the literature. For example, the use of different frequency sub-bands for each transmitted beam was proposed in [12], yielding a loss of axial resolution. In [13], MLT cross-talk in 3D images was lowered by properly choosing, based on the transducer array geometry, the directions of the simultaneous transmitted beams. Also harmonic imaging was demonstrated as a possible solution to obtain images with reduced cross-talk [14]. In [10] and [15], it was shown that

TX/RX apodization with Tukey windows allows good cross-talk rejection at the expense of a reduced lateral resolution. Similar performance was achieved with an approach based on Minimum Variance (MV) beamforming [16].

In this paper we propose the application of Filtered-Delay Multiply And Sum (F-DMAS) beamforming to high frame-rate imaging based on MLT. DMAS is a non-linear beamformer, originally introduced in microwave imaging [17], which has been recently modified by some of the authors for application to ultrasound B-mode imaging [18]. As shown in [18] [19], the new approach, called F-DMAS, can be used to improve the contrast resolution and clutter rejection by significantly lowering the pulse-echo beam side lobes and narrowing the main lobe.

The aim of this work is thus to analyze the performance of F-DMAS beamforming combined with MLT. In particular, it is shown that, compared to MLT with standard Delay And Sum (DAS) beamforming and TX/RX Tukey apodization:

1) an improved rejection of RX cross-talk is achieved;
2) images with improved lateral resolution and contrast are obtained even when the number of simultaneously transmitted beams is very high.

The paper is organized as follows. In Section II the MLT technique and F-DMAS algorithm are described. The simulation/experimental setup and the parameters used to evaluate image quality are also reported. Section III illustrates the results achieved both in simulations and experiments, on a tissue-mimicking phantom and *in vivo*. Finally, the performance of the proposed method is discussed in Section IV and some conclusive remarks are provided in Section V.

II. MATERIALS AND METHODS

A. Multi-Line Transmission

Let us consider N_{TX} beams transmitted into N_{TX} steering directions separated by a θ_{TX} angular distance, to cover a θ-degrees-wide field of view (i.e. $\theta_{TX}=\theta/N_{TX}$) [10] [16]. The TX beams are subsequently moved by the same angular step, θ_{STEP} (if N_{LINES} is the number of scan lines, then $\theta_{STEP}= \theta/N_{LINES}$), and the TX/RX process is repeated until all the image sector has been covered.

If for example $N_{TX} = 2$, two different focusing delay profiles have to be computed in order to focus along 2 different scan lines, i.e. one for each scan direction. The final excitation pulse, to be applied to each element of the transducer array, is thus obtained by summing up the voltage signals that would be required to separately focus along direction #1 and along direction #2 in standard Single Line Transmission (SLT) [10]. Then, the backscattered signals received by the transducers have to be beamformed in parallel along directions #1 and #2.

The main drawback of this technique is that the interference among the simultaneous beams generates the so-called cross-talk artifacts in the final image, which are more visible as the number of MLT beams increases. More specifically, two types of cross-talk can be identified: TX cross-talk, which is due to the interference between the side lobes of the TX beams and the main lobe of the RX beams, and RX cross-talk, which is instead due to the interference between the main lobe of TX beams and the side lobes of RX beams [10]. In practice, if we suppose to scan a single point scatterer to obtain the system Point Spread Function (PSF), the cross-talk artifacts appear in the image both along the range direction (TX cross-talk), just around the PSF intensity peak, and along the cross direction (RX cross-talk), at the two sides of the PSF peak. The RX cross-talk artifacts are usually far from the main lobe direction and they are located at multiples of θ_{TX}.

B. Filtered-Delay Multiply And Sum Beamforming

In F-DMAS non-linear beamforming, for the i-th scan line, the radio-frequency (RF) signals received by the n-th element are delayed according to the conventional dynamic focusing rule, to produce the signals $s_{n,i}(t)$. Then, the beamformed signal $y_i(t)$ is computed as:

$$y_i(t) = \sum_{n=1}^{N-1} \sum_{m=n+1}^{N} \hat{s}_{n,i}(t)\hat{s}_{m,i}(t), \quad (1)$$

where

$$\hat{s}_{n,i}(t) = sign\,(s_{n,i}(t)) \cdot \sqrt{|s_{n,i}(t)|}, \quad (2)$$

while N is the number of active elements. Subsequently, the $y_i(t)$ signal undergoes band-pass (BP) filtering: both baseband and second harmonic components originate from the multiplication stage, as the multiplied signals have similar spectral content; thus, the BP filter is designed to pass the second harmonics only and to attenuate the baseband and higher-frequency components.

As shown in [18], the described operations are very similar to the computation of the aperture spatial autocorrelation function. F-DMAS beamforming is based on a measure of the backscattered signal coherence and provides improved lateral/contrast resolution and noise rejection, as compared to conventional DAS (for an in-depth explanation of such aspects, please refer to [18]).

After each scan line has been reconstructed, envelope detection is performed by means of the Hilbert transform; finally, the image is normalized to its maximum value and logarithmically compressed for the final display.

C. Simulation and Experimental Setup

The performance of MLT with F-DMAS beamforming was compared to that of MLT with DAS beamforming. Several different scenarios were tested in both simulations and experiments, by implementing SLT and MLT with 4, 6, 8 or 16 beams (i.e. 4/6/8/16-MLT). In each case, the following beamformer and apodization-window configurations were considered: DAS with Tukey apodization (Tukey window α=0.5) in TX/RX (i.e. Tukey/Tukey), and F-DMAS with Tukey apodization in TX only (i.e. Tukey/Rect).

Simulations were carried out in Matlab (The MathWorks, Natick, MA) by using Field II [20] [21], considering a 128-element phased array (pitch=170 μm, height=1.2 mm) with a center frequency of 2 MHz and ~50% (-6 dB) fractional-bandwidth. In experiments, only the 64 odd elements of the phased array probe (model PA230, Esaote S.p.A., Florence, Italy) were used, as the ULA-OP system [22] (employed to

perform experimental acquisitions) features 64 independent TX/RX channels. The actual pitch was thus the double of the one available in the probe. Only the odd elements of the array were used in simulations too, in order to make the obtained results consistent.

The TX focus was set at a radial distance of 70 mm, while dynamic focusing was implemented in RX. A 90° image sector was acquired, including 192 image lines. The excitation signal was a 2-cycle Hanning-windowed sinusoidal burst at 2 MHz and the sampling frequency was set to 50 MHz. The received RF signals were BP-filtered between 0.5 MHz and 3.5 MHz, around their average center frequency. When F-DMAS was used, a BP filter, centered at twice the central frequency and with a similar fractional bandwidth, was applied to the beamformed lines by windowing their spectra between 1.5 MHz and 7 MHz with a 50% tapered Tukey window. The filter was designed to attenuate the baseband component and to pass the second harmonics only (which is also worth reducing the noise bandwidth), limiting ripple in the time domain too.

The aforementioned scan parameters were employed both for simulations and experimental acquisitions. Particularly, in the latter case, the pre-beamformed RF data from the 64 active channels of the ULA-OP were acquired at 12-bit resolution by a 36 GB memory board [23] and sent to a personal computer for off-line processing. The pre-beamforming signals were thus pre-filtered and then beamformed in Matlab. It is worth underlying that, since the maximum available amplitude with the linear transmitter of the ULA-OP system was limited to 25 Vpp, the actual amplitude of 4/6/8/16-MLT signal turned out to be reduced to 25 Vpp/4, /6, /8 and /16, respectively.

In simulations, the system PSFs at different depths were obtained by simulating the scan of 4 point scatterers in water, placed along the x=0 mm axis at 20-40-60-80 mm depth.

Similarly, experiments were performed by scanning 4 nylon wires (diameter 100 μm) placed at different depths in a water tank. A CIRS phantom model 040GSE (CIRS Inc., Norfolk, VA), including 4 anechoic cysts at 15-45-70-100 mm depth, two hyperechoic cysts at 30-115 mm depth and several wires, was also scanned.

In vivo acquisition of echocardiographic images were finally carried out; both 5-chamber and 4-chamber apical views of the heart of a young healthy volunteer were acquired by an expert cardiologist using the ULA-OP system.

D. Outcome Parameters

The quality of the MLT DAS/F-DMAS beamformed images was evaluated in terms of resolution, contrast and SNR. The spatial resolution was measured on the simulated PSF images, by computing the axial and lateral main-lobe size at -6 dB. The contrast ratio (CR) and contrast-to-noise ratio (CNR) were measured on the cyst phantom images; they were computed as follows:

$$CR = 20\,log_{10}\left(\frac{\mu_{cyst}}{\mu_{bck}}\right) \tag{3}$$

$$CNR = \frac{\left|\mu_{bck} - \mu_{cyst}\right|}{\sqrt{\sigma_{bck}^2 + \sigma_{cyst}^2}} \tag{4}$$

where μ_{cyst} and μ_{bck} are the mean image values measured on the envelope-detected signals (before log-compression), inside the cyst and in the background tissue, respectively (see Fig. 3a). σ^2_{cyst} and σ^2_{bck} are the corresponding variances.

Two more regions of interest were defined in the cyst phantom images: S_S, which is an area in the background tissue (also used for CR/CNR computation) just outside the cyst at 70 mm depth, and S_N, which is an area outside the phantom where only noise is expected (see Fig. 3a). Then, the SNR was computed as:

$$SNR = 10\,log_{10}\left(\frac{P_S}{P_N}\right), \tag{5}$$

where P_S and P_N are the average power of signal and noise, respectively.

To compute P_S, the useful signal contribution (which is expected not to vary during the acquisition time, as both the probe and the phantom are kept still during acquisitions) must be extracted from the image values present in S_S. To do so, the baseband signals in S_S over K=20 consecutive frames were used. If we consider one of these signals (whose value in frame k is denoted as i_k), then its mean over time/frames (i.e. only its DC component) must be calculated to extract the useful signal contribution, while reducing noise at the same time [24]:

$$\bar{i} = \left(\sum_{k=1}^{K} i_k\right) \Big/ K\,. \tag{6}$$

This operation was performed for all the image points in S_S. P_S was then computed by averaging the squares of such values, after envelope detection, over S_S:

$$P_S = \int_{S_S} \bar{I}^2 dS \Big/ \int_{S_S} dS \tag{7}$$

where $\bar{I}$ is the modulus of $\bar{\imath}$. P_N was instead directly computed by averaging the squares of all the envelope-detected image values I included in S_N over 20 frames:

$$P_N = \int_{S_N} I^2 dS \Big/ \int_{S_N} dS. \tag{8}$$

III. RESULTS

A. Simulated Point Spread Function

The results obtained by simulating the PSF in the considered configurations are resumed in Fig. 1 and Table I. Fig. 1 shows the beampatterns at a radial distance of 61 mm, and the axial profiles of the PSF along the 0° direction.

As expected, the lateral beampatterns clearly show the presence of RX cross-talk when MLT is applied: an increased number of simultaneously transmitted beams results in a higher number of side-lobes, as shown in Fig. 1a-b. Also the TX cross-talk becomes visible in the axial profiles in Fig. 1c-d. The application of TX/RX Tukey apodization, however, adequately limits the magnitude of both cross-talks. When F-DMAS is employed (Fig. 1b), not only the RX cross-talk level

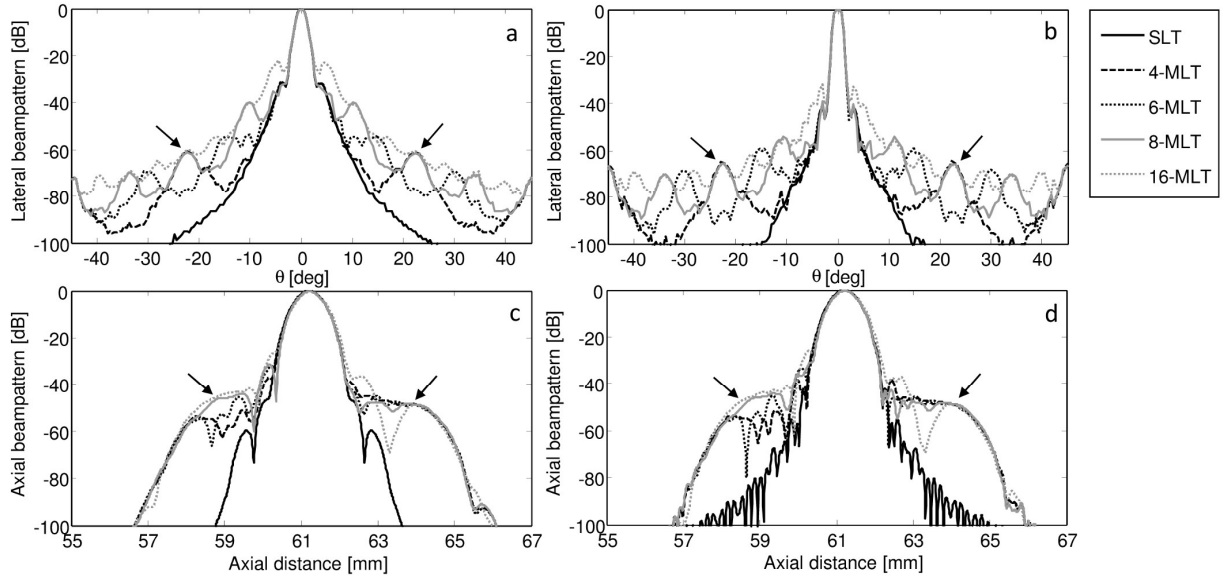

Fig. 1. Normalized lateral beampatterns of the simulated PSF at 61 mm distance (a, b) and axial profiles at 0° (c, d) obtained with DAS (a, c) and F-DMAS (b, d) in the considered configurations. With DAS, Tukey apodization is applied both in TX and RX, while only TX apodization is employed with F-DMAS. The arrows point out two examples of artifacts due to RX cross-talk (a, b) and TX cross-talk (c, d).

TABLE I
LATERAL AND AXIAL MAIN-LOBE BEAM WIDTHS [mm] AT -6 dB

		PSF at 20 mm		PSF at 40 mm		PSF at 60 mm		PSF at 80 mm	
		LBW	ABW	LBW	ABW	LBW	ABW	LBW	ABW
SLT	DAS T/T	1.38	0.42	2.19	0.92	2.62	0.86	3.43	0.85
	F-DMAS T/R	0.97	0.43	1.67	0.92	2.12	0.86	2.75	0.85
4-MLT	DAS T/T	1.33	0.41	2.21	0.92	2.64	0.86	3.44	0.85
	F-DMAS T/R	0.98	1.18	1.67	0.92	2.13	0.85	2.76	0.84
6-MLT	DAS	1.60	2.40	2.16	0.94	2.62	0.86	3.42	0.85
	F-DMAS T/R	1.01	2.35	1.66	0.93	2.12	0.86	2.74	0.84
8-MLT	DAS T/T	0.82	1.44	2.23	0.90	2.62	0.85	3.43	0.85
	F-DMAS T/R	0.72	1.53	1.68	0.91	2.12	0.85	2.75	0.84
16-MLT	DAS T/T	1.13	1.10	2.99	1.43	2.48	0.88	3.23	0.88
	F-DMAS T/R	0.81	1.07	1.85	1.44	2.03	0.88	2.62	0.88

LBW = lateral beam width at -6 dB; ABW = axial beam width at -6 dB. Transmit/Receive apodization: R = Rect, T = Tukey.

lowers if compared to DAS with RX Tukey apodization, but the main lobe is narrower, too. On the other hand, the TX cross-talk level with DAS and F-DMAS is almost equal.

The beam main-lobe widths reported in Table I show that, overall, the lateral beam width does not get significantly worse when the number of MLT beams increases. In addition, the results confirm that the lateral resolution is always better with F-DMAS than with DAS and Tukey apodization, as F-DMAS achieves a narrower main-lobe in all cases. No significant variations of the axial resolution at -6 dB can be observed in the analyzed configurations, except at the shallower depths where the PSF axial profile is rather irregular, presenting several peaks higher than -6 dB.

B. *Experimental Images of the Nylon Wires in a Water Tank*

Similarly to the simulated PSFs, the experimentally acquired images of 4 nylon wires in water (Fig. 2) confirm that the performance of F-DMAS with TX-only Tukey apodization is always better than that of DAS with Tukey apodization on both TX and RX.

Particularly, as the number or MLT beams increases, the RX cross-talk artifacts become more visible in the DAS images, since RX Tukey apodization does not suppress them as well as F-DMAS does. Also the noise is better rejected by F-DMAS. This is especially important in the case of MLT with a higher number of simultaneous beams, e.g. 8/16-MLT, since the amplitude of the transmitted signal is 8/16 times lower than in SLT, and thus the SNR is lower too.

The TX cross-talk is attenuated in a similar way by the two beamformers, thanks to TX Tukey apodization. Even if F-DMAS does not directly reduce the TX cross-talk, the improvement of the lateral resolution further limits its presence, by relegating the TX cross-talk to a narrower region compared to DAS (as also pointed out in [16] for MV beamforming).

Moreover, the resolution of F-DMAS images is better and the main lobes of the PSFs are narrower.

C. *Experimental Cyst Phantom Images*

Images of the CIRS phantom were acquired by scanning two different regions of interest, i.e. one centered on the anechoic cyst series and one including the two hyperechoic cysts. As an example, Fig. 3 shows the SLT and 4-MLT images of the anechoic cysts beamformed with F-DMAS and

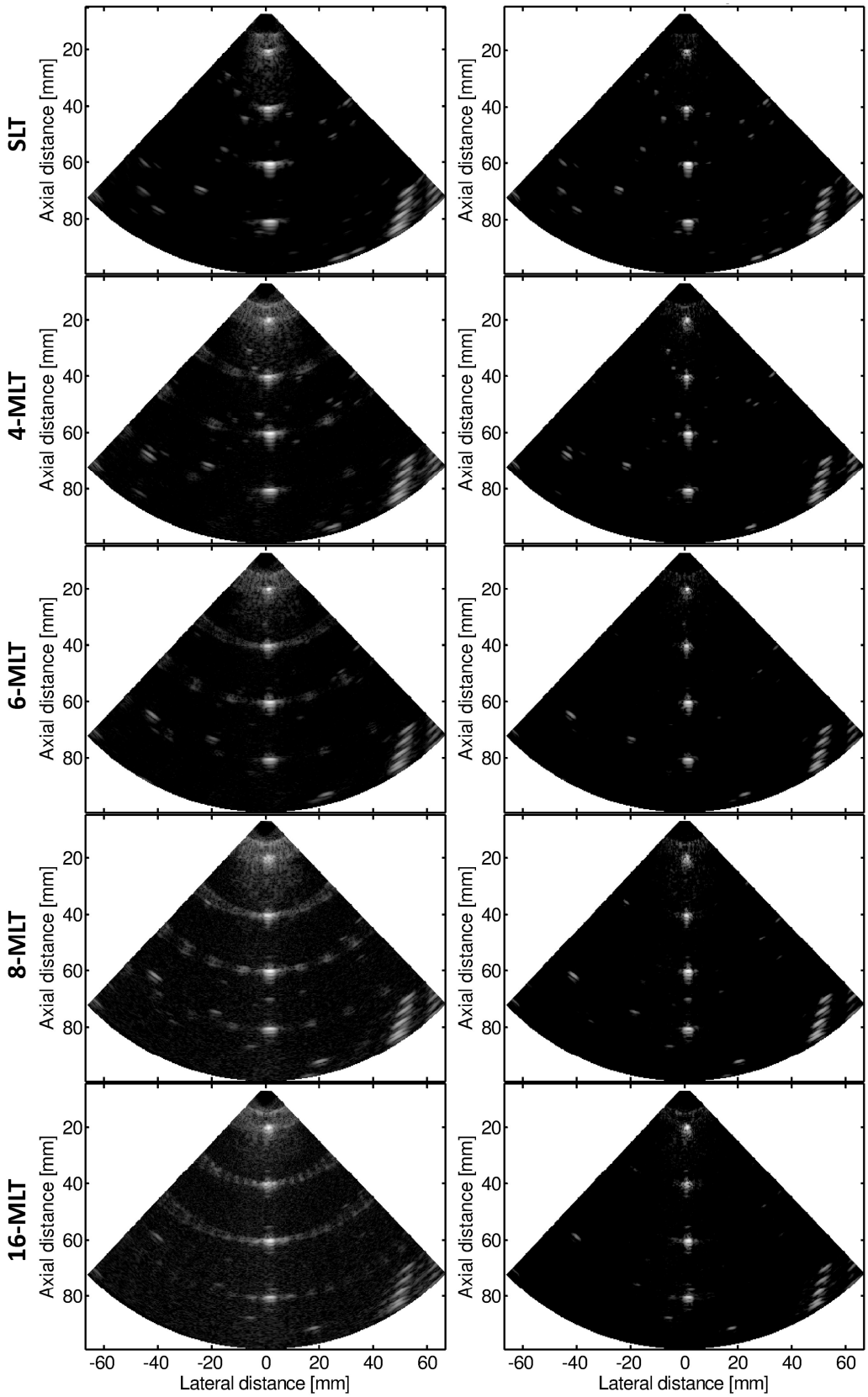

Fig. 2. Images of the nylon wires in a water tank acquired by performing SLT or 4/6/8/16-MLT with DAS (left column) and F-DMAS (right column) beamforming. Figures are displayed over a 60 dB dynamic range (log scale).

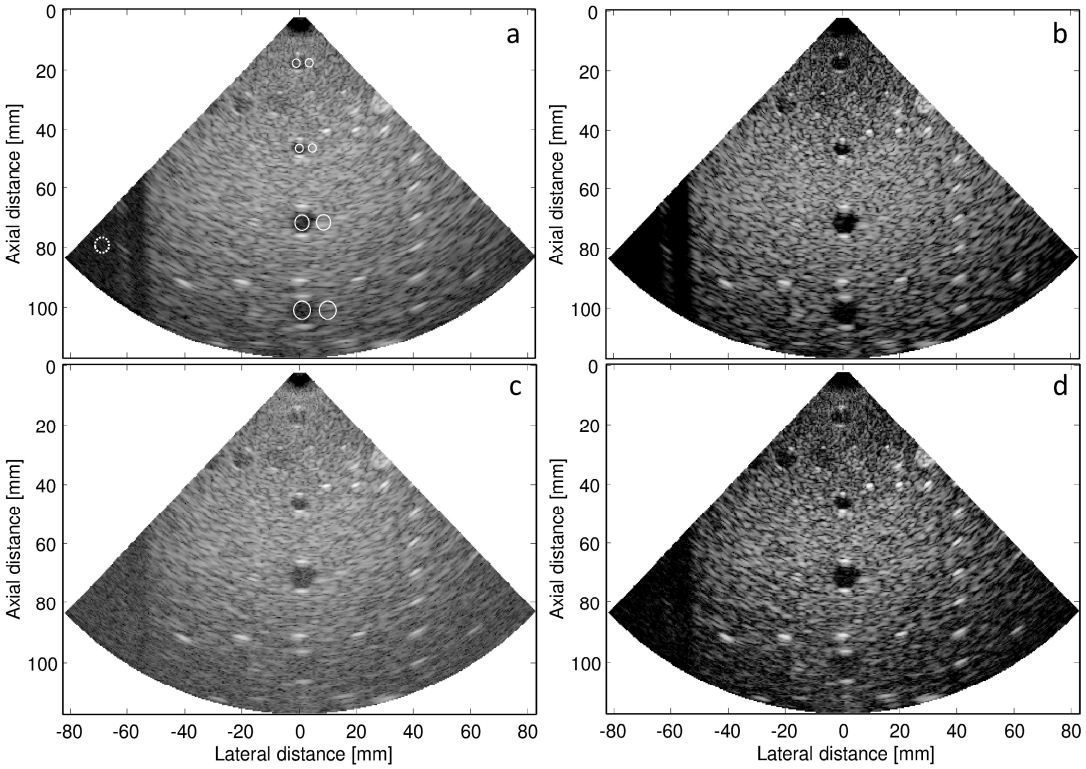

Fig. 3. Experimental cyst phantom images obtained by implementing SLT (a, b) or 4-MLT (c, d) with DAS (a, c) and F-DMAS (b, d) beamforming. Figures are displayed over a 60 dB dynamic range (log scale). White solid circles in (a) include the areas used for CR/CNR/SNR computation, as explained in Section II.D. For the SNR computation, also the area included in the white dotted circle was considered to evaluate noise power.

TABLE II
IMAGE QUALITY PARAMETERS MEASURED ON THE CYST PHANTOM IMAGES

		SLT		4-MLT		6-MLT		8-MLT		16-MLT	
Cyst	Parameter	DAS T/T	F-DMAS T/R	DAS T/T	F-DMAS T/R	DAS T/T	F-DMAS T/R	DAS T/T	F-DMAS T/R	DAS T/T	F-DMAS T/R
AC15	CR [dB]	-8.95	-17.89	-6.4	-10.53	-9.67	-15.72	-6.16	-12.38	-6.66	-11.63
	CNR	1.23	0.92	0.94	0.68	1.17	0.75	0.84	0.73	0.95	0.68
AC45	CR [dB]	-16.91	-24.40	-16.49	-26.17	-14.79	-21.32	-13.97	-22.46	-8.40	-11.97
	CNR	2.09	1.34	2.14	1.20	2	1.27	1.93	1.07	1.28	0.77
AC70	CR [dB]	-22.26	-32.48	-15.03	-22.37	-11.16	-13.71	-9.28	-14.42	-3.88	-4.56
	CNR	1.55	1.37	1.39	1	1.20	0.84	1.07	0.78	0.56	0.42
AC100	CR [dB]	-12.09	-21.39	-3.28	-10.19	-0.55	-2.19	-0.81	-4.27	2.95	3.47
	CNR	1.33	1.12	0.48	0.71	0.08	0.19	0.13	0.36	0.45	0.33
HC30	CR [dB]	14.70	21.02	14.72	21.49	14.53	22.18	15.09	20.55	14.05	19.93
	CNR	1.42	0.83	1.45	0.89	1.47	0.94	1.34	0.86	1.61	0.92
HC115	CR [dB]	14.26	19.55	10.22	20.09	8.86	18.11	7.73	15.94	5.48	13.90
	CNR	2.08	1.54	1.57	1.34	1.35	1.24	1.18	1.06	0.84	0.99
	SNR [dB]	28.24	44.90	17.71	32.16	14.28	26.45	11.78	23.78	5.02	13.73

AC = anechoic cyst, HC = hyperecoic cyst. The acronym AC/HC is followed by the cyst depth [mm]. TX/RX apodization: R = Rect, T = Tukey.

with DAS and Tukey apodization.

The performance parameters are reported in Table II; they include the CR and CNR measured in correspondence of all the anechoic/hyperecoic cysts (AC/HC), at 15-45-70-100 mm depth and at 30-115 mm depth, respectively. The SNR was measured using the envelope-detected image values in the tissue background, at 70 mm depth, and in an area outside the phantom (see Fig. 3a), over 20 consecutive frames.

Note that the hyperecoic cyst at 30 mm depth is also partially visible on the right side of the image sectors in Fig. 3; however, a second acquisition was performed in order to include both the hyperecoic cysts and to align them to the center of the sector, as previously explained.

Overall, the MLT F-DMAS images show higher contrast resolution compared to the DAS ones. With F-DMAS the anechoic cysts are darker and better defined; moreover, noise is better suppressed, as can be clearly seen inside the cysts and in the dark region outside the tissue phantom, on the left of the image sector. Also the wires and hyperechoic cysts are more clearly highlighted and better resolved.

The CR is always higher with F-DMAS and generally it decreases moving towards the shallower or farther depths, where also the difference between the CR obtained with DAS and F-DMAS attenuates. In the majority of cases, the CR obtained with F-DMAS and MLT with up to 8 beams is even higher than that achieved by DAS in the SLT case. At 45 mm

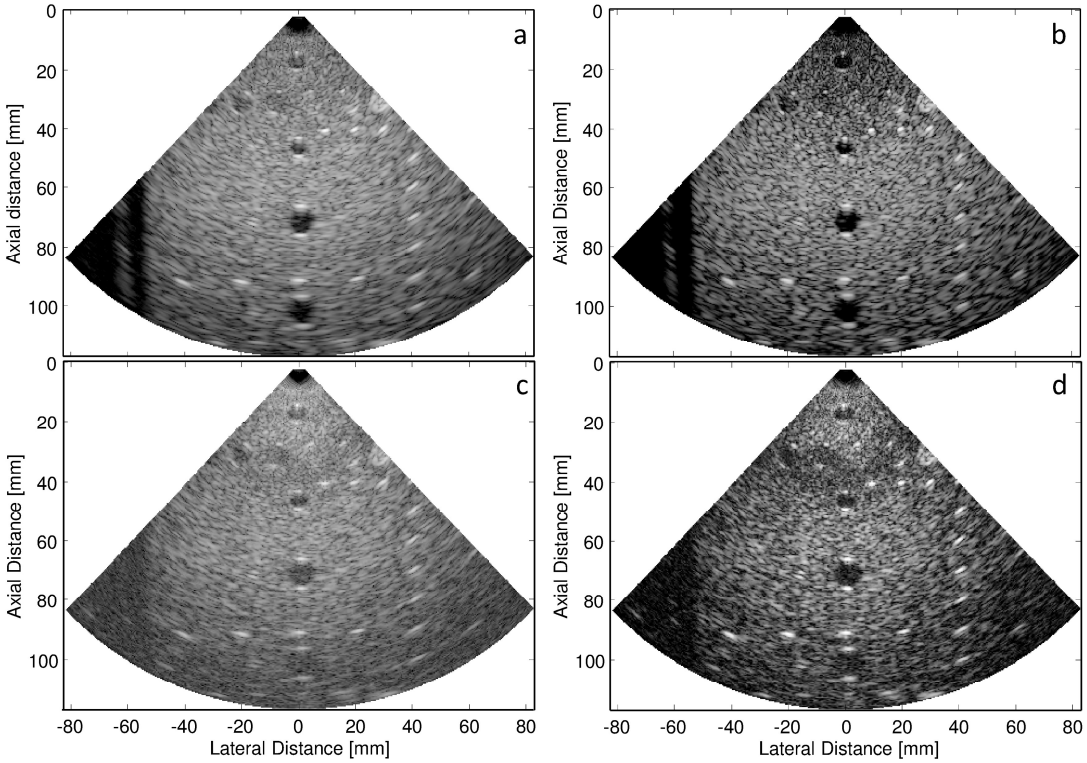

Fig. 4. Experimental cyst phantom images, with averaging over 20 frames, obtained by implementing SLT (a, b) or 16-MLT (c, d) with DAS (a, c) and F-DMAS (b, d) beamforming. Figures are displayed over a 60 dB dynamic range (log scale).

depth, for example, the CR with 4-MLT and 8-MLT F-DMAS is respectively ~9 dB and ~5.5 dB higher than with SLT DAS with Tukey apodization.

The CNR, which is related to the speckle pattern, is lower with F-DMAS; it gets higher near the focal depth and it generally lowers as the number of MLT beams increases.

On the opposite, the SNR is always higher with F-DMAS (i.e., from about +9 to +17 dB). Unfortunately, as in MLT the transmitted signal amplitude decreases proportionally to the number of simultaneous TX beams, the SNR also gets lower, and the cyst at 100 mm depth becomes hardly visible in all the MLT images, even in the F-DMAS ones, which are however clearer. In Fig. 3c the deeper cyst is almost covered by noise; also with F-DMAS (Fig. 3d) the image is noisy, but that cyst is still partially visible. Nevertheless, in a possible low-noise scenario, F-DMAS would allow to obtain good results even in the case of 16-MLT. This is shown by Fig. 4, in which the SLT and 16-MLT images, obtained by averaging the raw RF signals over 20 consecutive frames (before image reconstruction), are represented.

D. *In Vivo Cardiac Images*

Some *in vivo* images of the human heart acquired with MLT are presented in Fig. 5. Also standard SLT images with DAS are provided in Fig. 5c and Fig. 5f for reference.

The 4-MLT F-DMAS 5-chamber view in Fig. 5b has significantly higher contrast and resolution than both the 4-MLT and SLT DAS images in Fig. 5a, c: the lumen of both ventricles is particularly clear and their borders are better defined, as well as the mitral valve and the aortic root. Some artifacts are however still visible in the atria. Similar considerations apply to Fig. 5d-e that show an 8-MLT 4-chamber view. In fact, the chambers are all well visible and both the anterior and inter-atrial septum and mitral valve are more clearly highlighted with F-DMAS. Even when compared to the SLT DAS case (Fig. 5f), the 8-MLT F-DMAS image has a high quality.

The video clips of both the 4-MLT 5-chamber view (Video4MLT.avi) and 8-MLT 4-chamber view (Video8MLT.avi) are available as supplementary files. In each video, the frames obtained with DAS and TX/RX Tukey apodization are shown on the left, and on the right with F-DMAS and TX-only Tukey apodization. The video clips include also the ECG signal recorded during the ultrasound scan with the ULA-OP system.

IV. DISCUSSION

One of the main drawbacks of the MLT technique is the presence of the so-called TX/RX cross-talk artifacts, caused by interferences among the multiple transmitted beams. In [10] [15], Tukey apodization was proven to be the most effective method to reduce such artifacts, even though at the expense of both sensitivity and lateral resolution.

The solution proposed in this paper uses the F-DMAS beamformer, which allows achieving a narrower main lobe and lower side lobes thanks to a multiplication in both time domain, i.e. to the doubled center frequency of the beamformed signals, and space domain (an analysis on the contributions brought about by the different factors involved in the F-DMAS algorithm is presented in [18]). A similar effect was achieved in [14] by exploiting the second-harmonic

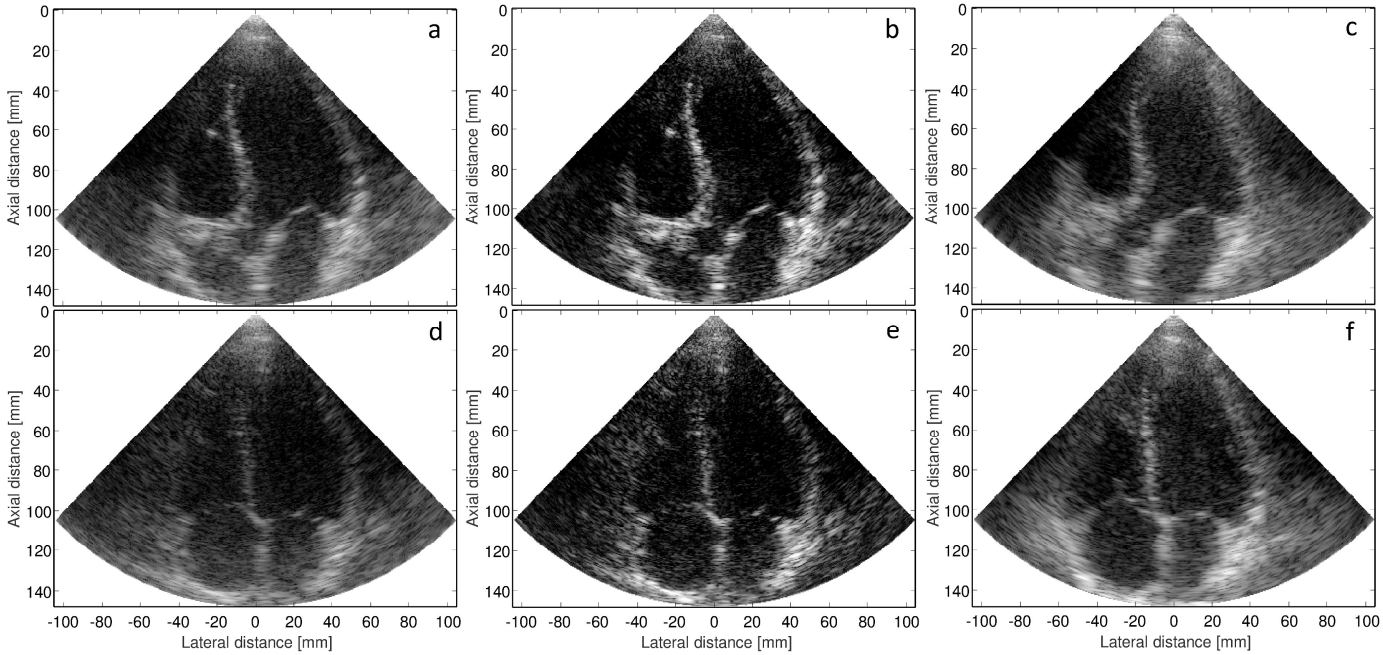

Fig. 5. *In vivo* heart images acquired by implementing 4-MLT (a, b) or 8-MLT (d, e) with DAS (a, d) or F-DMAS (b, e) beamforming. The figures represent a 5-chamber (a, b) and a 4-chamber (d, e) apical view, respectively. For both views, the reference SLT image obtained with DAS and Tukey apodization is also included on the right for comparison (c, f). Images are displayed over a 65 dB dynamic range (log scale). The video clips of 4-MLT and 8-MLT images (Video4MLT.avi and Video8MLT.avi) are available as supplementary files.

signals generated by nonlinear propagation, actually resulting in a reduction of MLT artifacts, particularly TX cross-talk. F-DMAS similarly brings to an improvement of contrast and lateral resolution, but with an effective rejection of RX cross-talk artifacts.

Both the simulated PSFs (Fig. 1) and the experimental images of the nylon wires in water (Fig. 2) show that RX cross-talk artifacts are better suppressed by F-DMAS than by DAS with Tukey apodization. Moreover, as shown in Table I, the application of Tukey TX apodization seems not to significantly affect the lateral resolution of the F-DMAS images. When F-DMAS is employed, the MLT images in Fig. 2 are very similar to the reference SLT one: RX cross-talk is only slightly significant (considering the display 60 dB dynamic range) and the lateral resolution is not degraded. As a matter of fact, the quality of the 16-MLT F-DMAS image in Fig. 2 is as good as, if not better, than that of the SLT DAS one. This also provides an experimental confirmation of the simulation results in Table I. Conversely, with DAS and Tukey apodization, RX cross-talk artifacts clearly appear in the images and increase together with the number of simultaneous TX beams, while the lateral resolution is lower than that achieved by both SLT and MLT F-DMAS. Moreover, the stronger background noise rejection further improves the overall quality of the F-DMAS images in Fig. 2.

It is however worth mentioning that, with the 340 µm pitch used in this work, grating lobes appear for the higher beam-steering angles in F-DMAS images, being the central frequency of received signals doubled. Nevertheless, these lobes have limited magnitude and do not compromise the image quality, as the presented results demonstrate. Such problem would be even more marginal if the full phased array, which actually has a pitch of 170 µm, were employed.

The better cross-talk suppression and resolution improves the quality of F-DMAS tissue phantom images compared to those achieved with DAS and Tukey apodization, also when MLT with a high number of TX beams is employed. The anechoic cysts are darker with F-DMAS, i.e. clutter is much more effectively removed, their borders are better defined, and the embedded wires look sharper. As Fig. 3 shows, contrast and resolution of the 4-MLT F-DMAS image are higher than those of both the SLT and 4-MLT DAS images. Furthermore, with F-DMAS the contrast and visibility of the gray-scale cyst targets (which are included in the phantom at ~30 mm depth and feature different scattering strengths) is improved too.

Quantitatively, the measured CR is always higher with F-DMAS (Table II), being the amount of such gain dependent on the number of MLT beams, depth and apodization. Even when 8 TX beams are employed, the CR obtained with F-DMAS is higher than that achieved by SLT DAS with Tukey apodization, except in the deeper regions where the MLT image becomes noisy. The SNR is always higher with F-DMAS too, since this beamformer is based on the computation of backscattered signal spatial coherence, that makes it able to better reject uncorrelated noise.

A drawback of this method is the lowering of CNR, due to the higher contrast resolution, which makes the speckle pattern look more defined and with more dark areas (as opposed to the quite uniform gray appearance of the DAS image speckle) [18] [25], especially when MLT is applied (which however occurs in the DAS case too).

As explained in Section III.C, the noise visible at higher depths in all the MLT images (e.g. Fig. 3c-d), particularly at higher number of MLT beams, is due to the low TX amplitude

which was used. In fact, in MLT the excitation pulses are superimposed to transmit several beams simultaneously, which implies that the array central element is excited with a higher voltage signal [10]. Therefore, in order to make the MLT acoustic output pressure almost equal to that of SLT, the excitation signal amplitude has to be N_{TX} times lower (where N_{TX} is the number of MLT beams) [15], which also lowers the SNR. In a higher-SNR scenario however, results like those in Fig. 4 could be obtained. Even if averaging the raw RF signals of 20 consecutive frames would not be feasible in a real-time application, Fig. 4d demonstrates that in such case F-DMAS could achieve a good image quality also with 16-MLT.

The *in vivo* results in Fig. 5 further confirm the improvement of resolution, contrast and definition of the heart anatomic structures in MLT images achieved thanks to F-DMAS, which allows to obtain an adequate image quality even when 8-MLT is employed.

A final comment should be made also on the computational cost of the proposed method. As shown in (2), a square root operation is carried out on every RF sample, with a possible impact on the overall complexity. However, in view of a real-time implementation, approximate solutions of the square root can be considered by employing Newton-Raphson's iterative methods [26], as already efficiently implemented on a low-end DSP for spectral Doppler ultrasound applications [27]. Moreover, current DSPs, e.g. the 320C6678 family (Texas Instruments, Austin, TX, USA), provide architecture-optimized instructions to compute 8-bit square roots in only one clock cycle. An accurate estimation of computational times however hasn't been performed yet. A real-time implementation of the F-DMAS algorithm is foreseen in future work.

V. CONCLUSION

In this paper the performance of the F-DMAS beamformer in high frame-rate ultrasound imaging with MLT was evaluated. The results achieved both in simulations and in phantom/*in vivo* experimental acquisitions show that F-DMAS provides a better suppression of RX cross-talk than DAS with Tukey apodization, improving the contrast, lateral resolution, target definition and background noise rejection at the same time, even when 16 simultaneous TX beams are employed.

This study demonstrates that F-DMAS makes it possible to achieve an up to 8-fold improvement of the frame rate in *in vivo* scans while still providing a high image quality.

ACKNOWLEDGMENT

The authors would like to thank Dr. G. Fradella (Careggi University Hospital, Florence, Italy) for his outstanding contribution in performing *in vivo* acquisitions.

REFERENCES

[1] G. R. Sutherland, G. Di Salvo, P. Claus, J. D'Hooge, B. Bijnens, "Strain and strain rate imaging: A new clinical approach to quantifying regional myocardial function," *J. Am. Soc. Echocardiogr.*, vol. 17, no. 7, pp. 788–802, 2004.

[2] R. Jasaityte, J. D'hooge, "Strain rate imaging: fundamental principles and progress so far," *Imaging Med.*, vol. 2, no. 5, pp. 547–563, 2010.

[3] A. Fenster, D. B. Downey, H. N. Cardinal, "Three-dimensional ultrasound imaging," *Phys. Med. Biol.*, vol. 46, no. 5, p. R67, 2001.

[4] M. Tanter and M. Fink, "Ultrafast imaging in biomedical ultrasound," *IEEE Trans. Ultrason., Ferroelectr., Freq. Control*, vol. 61, no. 1, pp. 102–119, 2014.

[5] J.-y. Lu, "2D and 3D high frame-rate imaging with limited diffraction beams," *IEEE Trans. Ultrason., Ferroelectr., Freq. Control*, vol. 44, no. 4, pp. 839-856, 1997.

[6] D. P. Shattuck, M. D. Weinshenker, S. W. Smith, O. T. von Ramm, "Explososcan: A parallel processing technique for high speed ultrasound imaging with linear phased arrays," *J. Acoust. Soc. Am.*, vol.75, no. 4, pp. 1273–1282, 1984.

[7] O. T. von Ramm, S. W. Smith, H. G. Pavey Jr., "High speed ultrasound volumetric imaging system II: Parallel processing and image display," *IEEE Trans. Ultrason., Ferroelectr., Freq. Control*, vol. 38, no. 2, pp. 109–115, 1991.

[8] G. Montaldo, M. Tanter, J. Bercoff, N. Benech, M. Fink, "Coherent plane-wave compounding for very high frame rate ultrasonography and transient elastography," *IEEE Trans. Ultrason., Ferroelectr., Freq. Control*, vol. 56, no. 3, pp. 489-506, 2009.

[9] J. Cheng, J.-y. Lu, "Extended high-frame-rate imaging method with limited-diffraction beams," *IEEE. Trans. Ultrason., Ferroelectr., Freq. Control*, vol. 53, no. 5, pp. 880-899, 2006.

[10] L. Tong, H. Gao, J. D'hooge, "Multi-transmit beam forming for fast cardiac imaging-A simulation study," *IEEE. Trans. Ultrason., Ferroelectr., Freq. Control*, vol. 60, no. 8, pp. 1719-1731, 2013.

[11] R. Mallart and M. Fink, "Improved imaging rate through simultaneous transmission of several ultrasound beams," *Proc. SPIE*, 1992, vol. 1773, pp. 120-130.

[12] L. Demi, J. Viti, L. Kusters, F. Guidi, P. Tortoli, M. Mischi, "Implementation of parallel transmit beamforming using orthogonal frequency division multiplexing-Achievable resolution and interbeam interference," *IEEE. Trans. Ultrason., Ferroelectr., Freq. Control*, vol. 60, no. 11, pp. 2310-2320, 2013.

[13] B. Denarie, T. Bjåstad, H. Torp, "Multi-line transmission in 3-D with reduced crosstalk artifacts: a proof of concept study," *IEEE. Trans. Ultrason., Ferroelectr., Freq. Control*, vol. 60, no. 8, pp. 1708-1718, 2013.

[14] F. Prieur, B. Dénarié, A. Austeng, H. Torp, "Multi-line transmission in medical imaging using the second-harmonic signal," *IEEE Trans. Ultrason., Ferroelectr., Freq. Control*, vol. 60, no. 12, pp. 2682-2692, 2013.

[15] L. Tong, A. Ramalli, R. Jasaityte, P. Tortoli, J. D'hooge, "Multi-transmit beam forming for fast cardiac imaging-Experimental Validation and in vivo application," *IEEE. Trans. Med. Imag.*, vol. 33, no. 6, pp. 1205-1219, 2014.

[16] A. Rabinovich, A. Feuer, Z. Friedman, "Multi-line transmission combined with minimum variance beamforming in medical ultrasound imaging," *IEEE. Trans. Ultrason., Ferroelectr., Freq. Control*, vol. 62, no. 5, pp. 814-827, 2015.

[17] H. B. Lim, N. T. Nhung, E. P. Li, N. D. Thang, "Confocal Microwave Imaging for Breast Cancer Detection: Delay-Multiply-and-Sum Image Reconstruction Algorithm," *IEEE Trans. Biomed. Eng.*, vol. 55, no. 6, pp. 1697-1704, 2008.

[18] G. Matrone, A. S. Savoia, G. Caliano, G. Magenes, "The Delay Multiply and Sum beamforming algorithm in ultrasound B-mode medical imaging," *IEEE Trans. Med. Imag.*, vol. 34, no. 4, pp. 940-949, 2015.

[19] G. Matrone, A. S. Savoia, G. Caliano, G. Magenes, "Ultrasound Plane-Wave Imaging with Delay Multiply And Sum Beamforming and Coherent Compounding," *Proc. IEEE Conf. Eng. Med. Biol. Soc. (EMBC)*, Orlando, FL, 2016, pp. 3223-3226.

[20] J. A. Jensen and N. B. Svendsen, "Calculation of pressure fields from arbitrarily shaped, apodized, and excited ultrasound transducers," *IEEE Trans. Ultrason., Ferroelectr., Freq. Control*, vol. 39, no. 2, pp. 262-267, 1992.

[21] J. A. Jensen, "Field: a program for simulating ultrasound systems," *Med. Biol. Eng. Comput.*, vol. 34, pp. 351-353, 1996.

[22] E. Boni, L. Bassi, A. Dallai, F. Guidi, A. Ramalli, S. Ricci, R. J. Housden, P. Tortoli, "A reconfigurable and programmable FPGA-based system for nonstandard ultrasound methods," *IEEE Trans. Ultrason. Ferroelectr. Freq. Control*, vol. 59, no. 7, pp. 1378 –1385, 2012.

[23] E. Boni, A. Cellai, A. Ramalli, P. Tortoli, "A high performance board for acquisition of 64-channel ultrasound RF data," *Proc. IEEE Ultrasonics Symp.*, Dresden, Germany, 2012, pp. 2067-2070.
[24] A. Ramalli, F. Guidi, E. Boni, P. Tortoli, "A real-time chirp-coded imaging system with tissue attenuation compensation," *Ultrasonics*, vol. 60, pp. 65–75, 2015.
[25] J. F. Synnevåg, A. Austeng, S. Holm, "Benefits of Minimum-Variance beamforming in medical ultrasound imaging," *IEEE Trans. Ultrason., Ferroelectr., Freq. Control*, vol. 56, no. 9, pp. 1868-1879, 2009.
[26] N. Louvet, J. M. Muller, A. Panhaleux, "Newton-Raphson algorithms for floating-point division using an FMA," *Proc. 21st IEEE International Conference on Application-specific Systems, Architectures and Processors*, Rennes, France, 2010, pp. 200–207.
[27] S. Ricci, R. Matera, A. Dallai, "Amplitude and phase estimator for real-time biomedical spectral Doppler applications," *Proc. IEEE International Conference on Acoustics, Speech and Signal Processing (ICASSP)*, Florence, Italy, 2014, pp. 5149–5152.